Reconsidering Sparse Sensing Techniques for Channel Sounding using Splicing

Sigrid Dimce *Student Member, IEEE*, Anatolij Zubow *Senior Member, IEEE*, Alireza Bayesteh, Giuseppe Caire *Fellow, IEEE*, and Falko Dressler *Fellow, IEEE*

Abstract—Multi-band splicing offers a promising solution to extend existing band-limited communication systems to support high-precision sensing applications. This technique involves performing narrow-band measurements at multiple center frequencies, which are then combined to effectively increase the bandwidth without changing the sampling rate. In this paper, we introduce a mmWave channel sounder based on multi-band splicing, leveraging the sparse nature of wireless channels through compressed sensing and sparse recovery techniques for channel reconstruction. We focus on three sparse recovery methods: the widely used grid-based orthogonal matching pursuit (OMP) algorithm as a baseline, our newly developed two-stage mmSplicer algorithm, which extends the OMP method by introducing an additional stage for improving its performance for our application, and our adaptation of sparse reconstruction by separable approximation (SpaRSA), named Net-SpaRSA, optimized for wireless applications. All three algorithms are integrated into an experimental OFDM-based IEEE 802.11ac system. Our analysis centers on evaluating the performance of these algorithms under limited number of narrow-band measurements, demonstrating that accurate CIR estimation is achievable even using only 50% of the full wideband spectrum. Additionally, we analyze and compare the computational complexity of these algorithms to assess their practical feasibility.

Index Terms—Channel splicing, multi-band splicing, channel sounder, joint communication and sensing, software-defined radio, OFDM, Wi-Fi

1 INTRODUCTION

Joint communication and sensing (JCAS) is becoming more important in different application domains, both in 6G as well as for the internet of things (IoT) [1]–[4]. This triggered ongoing discussions of appropriate waveforms, with orthogonal time frequency space (OTFS) being considered a possible compromise [5]. However, most existing communication systems are based on orthogonal frequency division multiplexing (OFDM), so, integrating sensing here is important [6]. Communication systems, like WiFi, extract channel state information (CSI), which is also utilized for sensing applications [7]. In traditional WiFi communication systems, CSI is extracted primarily for equalization purposes, where

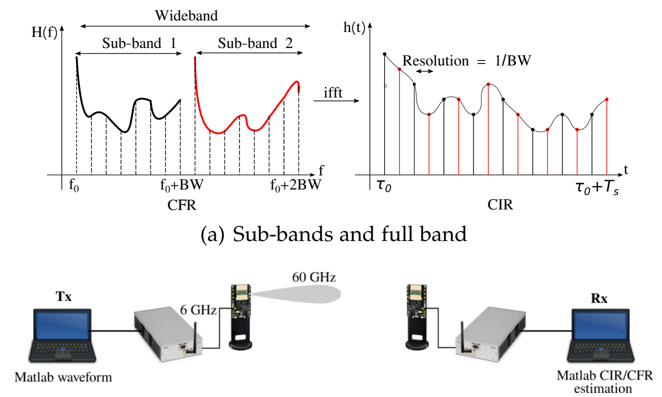

(a) Sub-bands and full band

(b) Channel splicing prototype

Figure 1. Illustration of the channel splicing concept and the experimental SDR-based setup.

high-precision multipath parameter estimation is not as crucial. However, for sensing applications using CSI [8]–[13], it is essential to accurately distinguish between closely spaced multipath components and estimate their parameters, such as time delay and magnitude, with high accuracy.

To separate multipath components that arrive close to each other, high delay domain resolution is required. The resolution is determined by $1/BW$, which, when multiplied by the speed of light, gives the minimum distance between two paths for them to be distinguishable at the receiver. For instance, a bandwidth of 20 MHz implies that two distinct paths must differ by at least 15 m in travel distance to be distinguishable [14]. One promising method to increase the effective bandwidth without modifying the device's supported sampling rate is multi-band splicing, also referred to as channel splicing in the literature [8]–[10], [14]–[16]. Conceptually, this involves measuring several narrow-band channels (referred to as sub-bands in this paper) and combining the results to simulate the effect of a single wideband measurement, as illustrated in Figure 1(a).

Multi-band splicing algorithms can be divided into three primary categories: maximum likelihood-based methods, subspace-based estimation methods, and compressed sensing techniques [17]. The traditional approach to estimating delay parameters relies on maximum likelihood-based methods, with the space-alternating generalized expectation-maximization (SAGE) [18] algorithm being

Sigrid Dimca, Anatolij Zubow, Giuseppe Caire and Falko Dressler are with the School of Electrical Engineering and Computer Science, TU Berlin, Germany; E-Mail: {dimce, zubow, dressler}@tkn.tu-berlin.de, caire@tu-berlin.de.
Alireza Bayesteh is with Huawei, Canada; E-Mail: alireza.bayesteh@huawei.com.
This work was supported by the Federal Ministry of Education and Research (BMBF, Germany) within the 6G Research and Innovation Cluster 6G-RIC under Grant 16KISK020K.

widely used. These methods are robust to noise and provide high-precision parameter estimation, though they are prone to converging to local optima [19]. Efforts to resolve this issue [20], [21], often result in algorithms with high computational demands. Other approaches in the literature tackle the multi-band delay estimation problem using subspace-based methods. For example, the classical multiple signal classification (MUSIC) algorithm [11] or variations utilizing multiple shift invariance structures [9], [22]–[24] in multi-band systems have been explored. These methods offer lower computational complexity but generally require a large number of snapshots to perform effectively.

Compressed sensing methods, on the other hand, leverage the sparsity of the channel impulse response (CIR) in the time domain—where only a few coefficients are non-zero or near zero. Research has demonstrated that the wireless multipath channel in an OFDM systems exhibit sparsity, making compress sensing applicable for time-delay estimation [25]. To illustrate sparsity in an OFDM system, we plot the CIR generated from our measurements at 2.4 GHz and 60 GHz, as shown in Figure 2. For each plot, we establish a magnitude threshold to distinguish strong multipath components (MPCs). This threshold, represented by a dotted black line, is set at 10% of the mean magnitude of the strongest path, in this case the line of sight (LoS) path. Paths with an amplitude exceeding this threshold are categorized as strong. The 10% threshold is empirically derived from our wireless experimental data, providing a balanced criterion for identifying significant MPCs while filtering out less relevant components. The plots indeed indicate that only a few components carry significant energy, and this number decreases even further at 60 GHz. Compressed sensing applies sparse recovery algorithms to the measured channel frequency response (CFR) samples across multiple sub-bands to reconstruct the wideband CIR [7][8], [14], [26]–[29]. This approach allows to accurately reconstruct the channel response from fewer measurements than required by traditional sampling methods, which is efficient in terms of bandwidth usage. However, these methods can become computationally expensive for large-scale problems.

The developed multi-band splicing algorithms have been applied in various fields, including localization [8], [9], [11], [14], [22], [26], [27], [30], [31], human [7], [13] and respiratory sensing [32], [33]. These applications are relevant for IoT and next-generation wireless systems, where accurate positioning and environmental sensing play a critical role.

Nevertheless, spectrum availability is highly dynamic, particularly in shared bands (e.g., ISM bands) and even in licensed spectrum due to increasing congestion. Parts of the spectrum often experience sporadic unavailability, and adjacent sub-bands may be occupied by other users or applications, making contiguous wideband access challenging. As shown in Figure 3, even acquiring a single 160 MHz of contiguous spectrum over time is difficult. This challenge has also been confirmed by a spectrum monitoring study [34], which demonstrated the benefits of non-contiguous channel bonding in dense environments such as stadiums, highlighting its flexibility and efficiency over contiguous bonding.

Such spectrum fragmentation poses a significant limitation for next-generation wireless systems, particularly in

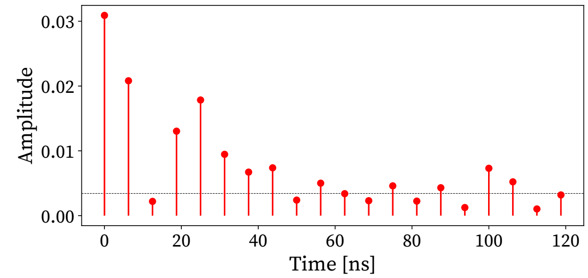

(a) CIR at 2.4 GHz

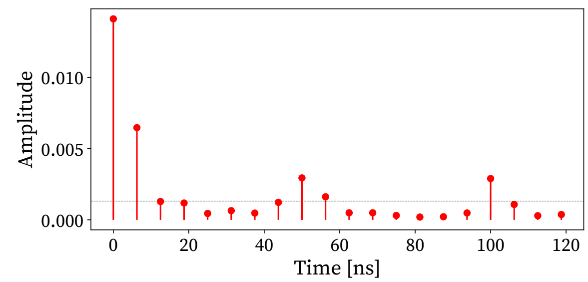

(b) CIR at 60 GHz

Figure 2. Illustration of the sparsity of the CIR at 2.4 GHz and 60 GHz along with the magnitude threshold to identify the strong MPCs.

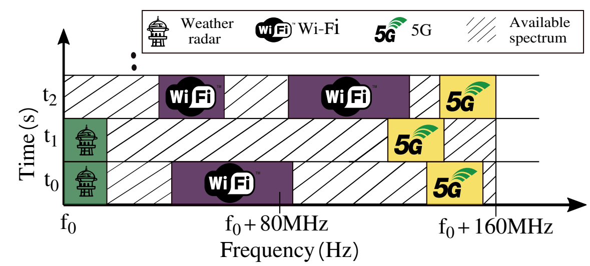

Figure 3. Illustration of the changing spectrum availability over time.

applications requiring high-resolution sensing and localization. This challenge is especially critical for emerging 5G/6G networks and IoT applications, where precise positioning and environmental awareness are essential. In fact, one of the key objectives of 3GPP 6G and future Wi-Fi standards is to integrate wireless communication with radar sensing capabilities. However, achieving the desired centimeter-level ranging resolution in 6G is restricted by the limited bandwidth available in current communication systems [26]. As mentioned in [26], even wideband 5G-NR and IEEE 802.11ay (WiGig) channels, with bandwidths of 400 MHz and 1.76 GHz, respectively, can only provide ranging resolutions of approximately 37 cm and 17 cm. In this scope, multi-band splicing offers a promising approach to overcome these limitations by effectively combining non-contiguous spectrum fragments, thus enabling high-resolution sensing and localization in practical deployments.

Numerous studies [9], [22], [23], [30], [35] have evaluated the effectiveness of the developed algorithms in estimating the time of arrival (ToA) or resolution limit [36] by deriving the Cramer-Rao lower bound (CRLB). The CRLB, calculated as the inverse of the Fisher information matrix (FIM), represents the absolute lower bound on the variance of an unbiased estimator. These studies have consistently shown that multi-band splicing across non-consecutive bands yields better performance than when applied to consecutive bands. However, according to [36], the frequency band aperture (i.e., the separation between the center frequencies of two consecutive bands) should remain within 20% of the carrier frequency to avoid significant frequency-dependent effects. Although the impact of frequency band aperture has been primarily examined through simulations, a comprehensive theoretical analysis is still needed.

Building on the theoretical foundations of multi-band splicing [14], [19], [27], the concept has matured significantly and many experimental prototypes have been presented [8], [10], [37]. Most current work on splicing is centered at low frequency bands (i.e., 2.4 GHz and 5 GHz). However, as these bands become increasingly congested due to the growing number of connected devices, recent studies are exploring the application of multi-band splicing in the millimiter-wave (mmWave) frequency band [26], [28], [38]. Despite the large available bandwidth, there are several challenges related to the mmWave band, including phase noise-where oscillators at high frequencies exhibit higher noise power spectral density, and the increased bandwidth contributes to phase distortion. Channel coherence time also reduces significantly. For instance, at 60 GHz the channel coherence time is reduced by a factor of $30\times$ for a mobility speed of just 2 m/s compared to the one at 2 GHz. Hence, in the context of splicing this would require reducing the number of jumps to different center frequencies and still estimating the wide channel accurately. Beyond these challenges specific to the mmWave frequency band, a key issue with multi-band splicing is the phase offset caused by transceiver impairment. This offset makes the direct concatenation of raw CFR samples infeasible. Therefore, it is essential to estimate and compensate for this offset in each sub-band before applying splicing. Several existing studies have tackled this challenge, which introduces additional coordination overhead [8], [11], [14], [32], [39]–[41].

In this paper, we present a mmWave channel sounder based on multi-band splicing, employing compressed sensing and sparse recovery techniques for channel reconstruction. Channel sounding is a method used to acquire knowledge on the properties of a communication channel. In this process, a known reference signal is transmitted through the channel, and the received signal is analyzed to understand how the channel has affected it [42]. By extracting metrics such as CIR (time domain) and CFR (frequency domain) changes in the signal such as distortions, delays and amplitude variations are examined. These parameters provide valuable insights into the channel's characteristics, such as path loss, multipath propagation, and fading, which are crucial for optimizing and designing wireless communication systems. In our previous work [37], we used the grid-based orthogonal matching pursuit (OMP) algorithm [14] for channel splicing, which had a good time resolution. We extended OMP to a two-stage algorithm, mmSplicer, to improve its applicability in wireless systems [28]. As an alternative approach, we adapted the Sparse Reconstruction by Separable Approximation (SpaRSA) algorithm [43], which is a well known sparse recovery techniques used in image processing, for use in wireless communications, labeled as Net-SpaRSA in the following.

We integrated all three algorithms into a communication system compliant with IEEE 802.11ac standard. The channel estimation is performed according to the least square (LS) estimation technique both in the time and frequency domain. Our splicing-based channel sounder is designed to work with software defined radios (SDRs), specifically Universal Software Radio Peripheral (USRP) X310, for transmitting/receiving the signal over the air, and the phased array antennas for up-converting the signal at 60 GHz (cf. Figure 1(b)). We demonstrate the practical use of the multi-band splicing technique at low frequencies (in simulations and indoor experiments) and at 60 GHz by applying the algorithm over narrow-band measurements and then comparing the estimated channel towards the full channel CIR. We deliberately use only 50% of the overall spectrum to evaluate the algorithms' performance in cases where parts of the spectrum are occupied or coherence time limits measurement across all sub-bands. Additionally, we briefly examine how the sub-bands distribution affects the algorithms' outcomes. Finally, we analyze the complexity of the algorithms in terms of execution time and computational cost, which is crucial for comparing different approaches. In summary, our results build the basis for OFDM-based JCAS solutions and for low-cost channel sounding.

Our main contributions can be summarized as follows:

- The OMP channel splicing algorithm is extended to a two-stage technique, mmSplicer, enhancing its applicability in wireless systems.
- The well-known SpaRSA algorithm is adapted to work in wireless communication scenarios and realized the Net-SpaRSA system for channel splicing.
- A practical OFDM communication system, based on IEEE 802.11ac, is implemented with an LS-based receiver for experimental evaluation, computing both the CIR and CFR in an SDR-based setup.
- The performance of OMP, mmSplicer, and Net-SpaRSA is experimentally evaluated across different frequency bands, utilizing only 50 % of the available spectrum.
- The algorithms are analyzed in terms of execution time and computational complexity.

The rest of the paper is structured as follows. Section 2 provides an overview of related works. Section 3 offers an in-depth presentation of OMP, our two-stage mmSplicer, and Net-SpaRSA. We then introduce the practical implementation used for lab experiments in Section 4. For validation, we obtained numerical results through simulations, cables and over-the air measurements as described in Section 5. In Section 6, we present our experimental results for channel splicing at mmWave frequencies. The execution time and computational complexity of the algorithms are analyzed in Section 7. Finally, Section 8 discusses identified challenges and Section 9 concludes the paper.

Notation: Throughout the paper, scalars are represented by letters, vectors and matrices are indicated in bold font.

2 Related Work

Multi-band splicing is a promising solution to increase effective transmission bandwidth without altering the device's sampling rate. Conceptually, the technique combines measurements over multiple narrow bands, either sequentially or across different frequency bands. The state of the art in multi-band splicing is provided in [17]. Our preliminary work [28] introduced a 60 GHz channel sounder that leverages multi-band splicing and a sparse recovery technique for scanning the communication channel.

Channel sounding is a crucial technique for acquiring knowledge to characterize the wireless channel within a certain frequency band [42]. The principle of sounding is to transmit a known baseband signal up-converted at the frequency of interest. Subsequently, on the receiver side, post-processing techniques are applied to extract metrics (CIR, CFR) that provide channel information. Over the years, several sounding techniques were developed with the sole purpose to accurately characterize the propagation channel. The two most common techniques are the spread spectrum sliding correlator [44] and the OFDM-based system [45]. Both techniques have demonstrated undeniable success at lower frequencies, as well as at mmWave frequency bands [46], [47].

In OFDM-based systems, the signal consists of multiple subcarriers, each observing the channel as flat, which mitigates the frequency selectivity issues of wideband transmission. Nevertheless, the system requires a large peak-to-average-power ratio (PAPR) as well as tight receiver synchronization [45]. Alternatively, the spread spectrum sliding correlator “spreads” the signal over a large bandwidth by mixing it with a binary pseudo noise (PN) sequence [44]. The received signal is mixed with a slower identical version of the PN sequence, which makes the system less vulnerable toward interference, but more complex in terms of hardware and software implementation compared to the OFDM system. Thus, choosing between these techniques depends on the application’s specific robustness and complexity requirements.

Propagation information is provided in the delay and frequency domain through the computation of the CIR and CFR, respectively, using various channel estimation techniques. Among these methods, the LS estimation is the most common method characterized by low computational complexity. Yet, in a few application scenarios, this technique yields inferior performance. Another well-known estimation method is the minimum mean square error (MMSE) [45], which minimizes the channel estimation error. However, MMSE leads to high computational complexity and requires prior channel statistic information, which sometimes is not available. Beside these traditional techniques, new models based on machine learning are being developed [48], [49], leading to an improved estimation performance.

Nevertheless, choosing the right channel estimation technique is also a function of the utilized hardware. For instance, low-resolution analog to digital converters (ADCs) require different estimation techniques due to the distortion they introduce to the original received signal. Employing low-resolution ADCs with large antenna arrays has drawn significant attention in mmWave systems. The authors in [50] propose a grid-less quantized variational Bayesian channel estimation algorithm, which has demonstrated optimal results in simulations. Grid-less estimation approaches are also explored in other works, such as [51] and [52]. In [51], the authors jointly estimate the channel, the carrier frequency offset (CFO), and perform data decoding, while in [52], the focus is on estimating and detecting line spectra in noisy environments.

In some OFDM systems, a combined approach using a PN sequence with OFDM has been adopted to improve channel characterization and synchronization. This approach, seen in the time domain synchronous OFDM (TDS-OFDM) system inserts a known PN sequence in the time domain before the data symbols, serving both as a guard interval for multipath channels and as a training sequence for synchronization and channel estimation [53]–[55]. Unlike conventional OFDM, TDS-OFDM does not require pilot subcarriers in the frequency domain, leading to improved spectrum and energy efficiency. Several studies have explored the combination of TDS-OFDM with compressed sensing to enhance channel estimation. For instance, the authors in [53], exploit the sparse nature of the underwater acoustic channel to apply the sparse recovery greedy algorithm of look-ahead backtracking orthogonal matching pursuit algorithm to estimate the channel. In [54] the authors propose a new channel estimation technique that uses the time-frequency training form. The PN sequence (time domain training) is used only for coarse channel path delay estimation, while pilots within the OFDM block are used for precise CIR estimation. Using the sparse nature of the channel, the number of pilots required is very small 1% of the total subcarrier number. In [55] the authors focus on TDS-OFDM combined with structured compressed sensing. This study used multiple small, inter-block-interference-free regions to perform multi-channel reconstruction, taking advantage of both channel sparsity and the observation that path delays change more slowly than path gains.

In this work, we focus on the traditional cyclic prefix OFDM (CP-OFDM) system, which utilizes a cyclic prefix as a guard interval, and leverage existing commodity WiFi devices to support sensing applications. These applications, however, require high-resolution CIR, a capability that cannot be achieved with WiFi devices due to their limitations in supported bandwidth.

Prior work exploited the sparse nature of the CIR in OFDM systems, applying compressed sensing and sparse recovery techniques to reconstruct wideband channels from sub-band measurements [7],[8], [14], [26]–[29], [37], [38], [56]. These works target mostly localization/ranging application [7],[8], [14], [26], [27] and channel sounding [28], [37]. For instance, Chronos [8] is an indoor positioning system that leverages compressed sensing techniques to estimate sub-nanosecond time of flight (ToF) across multiple frequency bands, focusing only on ToF rather than full CIR estimation. In [27], a localization technique is presented that overcomes hardware phase offsets through a phase retrieval scheme using CSI magnitude values alone for CIR estimation, with an enhanced version described in [14]. This version applies atomic norm denoising to estimate and remove per-band linear phase distortions before concatenating samples and using OMP to estimate high-resolution CIR, resolving ambiguity via a handshaking protocol. HiSAC [26], is a JCAS system utilizing multiple technologies (e.g., 5G-NR and WiGig) and non-contiguous bands. Unlike the aforementioned works operating at low frequencies (2.4–7.1 GHz), HiSAC operates at 60 GHz, achieving a 20-fold improvement in resolution compared to single-band scenarios. Most recently, CCS-FI [7] is proposed as a system that sparsely samples the channel in the frequency domain, and uses compressive sensing to widen the effective sensing bandwidth of Wi-Fi. The authors propose a deep-learning-based approach for sparse recovery of the channel, which improves ToF and angle of arrival (AoA) estimation. This enhancement enables higher accuracy in distance measurement and spatial resolution, facilitating applications such as multi-person differentiation.

Many of the cited works address hardware distortions within their algorithms, which remains a core challenge in multi-band splicing; hardware imperfections yield to a time and phase offset in each sub-band, which requires to be estimated and compensated before concatenating the data from different sub-bands. However, none of the works to date have analyzed the performance of their algorithms under varying spectrum loads or considered coherence time impacts especially at high frequencies.

In this paper, we present a multi-band splicing based channel sounder, which builds upon existing hardware for scanning the bandwidth at 60 GHz. We adapt the sparse recovery algorithm SpaRSA [43] for our channel splicing application, referring to it as Net-SpaRSA throughout. Furthermore, we integrated OMP, our newly developed two-stage mmSplicer and Net-SpaRSA in an OFDM communication system. Our setup is validated in simulation and indoor experiments, at sub-6 GHz and 60 GHz. Deliberately, we try to assess CIR using only 50 % of the overall spectrum, considering the possible impact of the channel coherence time and spectrum load. Additionally, we briefly examine the effect of spectrum fragmentation on the performance of each algorithm and analyze their execution time and computational complexity. This allows to obtain completely new insights into the behavior of splicing techniques. Our implementation of the algorithms, along with the experimental data collected in this study, is publicly available to the research community.[1]

3 Algorithms

This section provides an overview of the sparse recovery algorithms used to reconstruct the sparse CIR from a set of narrowband measurements that together represent 50% of the estimated bandwidth (cf. Figure 1). We deliberately focus on compressed sensing over maximum likelihood-based and subspace-based estimation methods due to its ability to estimate the complete channel response by sampling only a few frequency bands, rather than requiring the entire spectrum. This advantage aligns with our goal of accounting for channel coherence time and spectrum load when determining the number of narrowband measurements that can be performed.

3.1 Two-Stage Spectrum Splicing Architecture for Multi-band Delay Estimation

The two-stage multi-band splicing algorithm (mmSplicer) builds upon the well-known sparse recovery OMP method, which is a computational efficient algorithm compared to more complex iterative algorithms in the literature [57]. However, the OMP model requires a predefined stopping condition (signal sparsity), which is often unknown in practical scenarios and is prone to errors [58]. To mitigate these limitations in real communication systems, an additional stage is introduced. This stage establishes a dynamic stopping condition, considering only estimated paths within a specified interval. An illustration of the algorithm is presented in Figure 4, and each stage of the algorithm is briefly described below.

[1]https://github.com/tkn-tub/sparse-recovery-channel-sounding

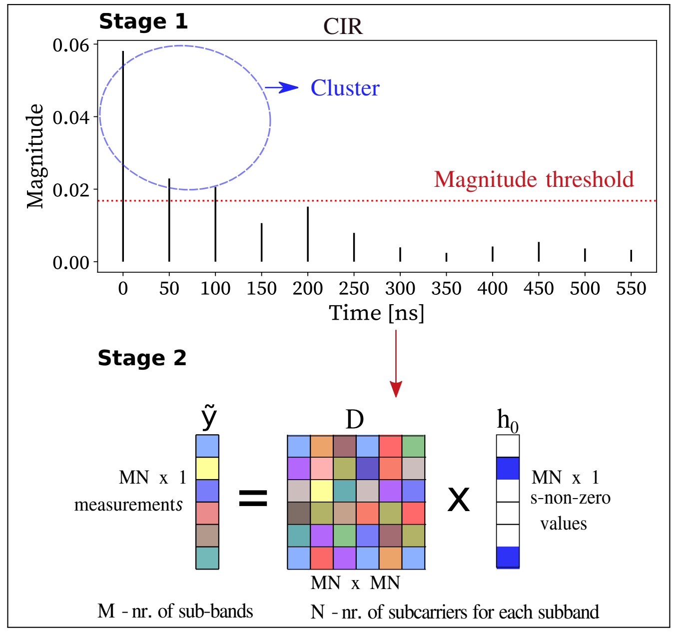

Figure 4. Overview of the proposed mmSplicer algorithm. The algorithm consists of two stages: Stage 1 uses a narrowband CIR measurement to identify clusters of strong MPCs that are both above a threshold and located in close proximity in the time domain. In Stage 2, this prior information is used to initialize the OMP algorithm across all the collected CFR samples, enabling accurate reconstruction of the wideband CIR.

3.1.1 Stage I: Clusters identification

The first stage of the algorithm analyzes the estimated CIR from a single sub-band to identify *clusters* of strong MPCs. These clusters are formed by grouping peaks that are both closely spaced (within two samples) and have magnitudes exceeding a threshold set at the 90th percentile (as shown in Figure 4). The reason behind this step is that although a narrowband signal offers limited resolution, it still captures the dominant paths. When a wider-band signal is used in the second stage, it can potentially reveal additional MPCs within these same time intervals, that is, it can resolve finer structure within clusters already seen in the narrowband. If no significant path is observed at a given delay in the narrowband CIR, then it is unlikely that a strong MPC exists there, because such a component would already have been visible, even at lower resolution. Therefore, this step allows us to pre-select the time regions of interest where dominant MPCs may reside. The number of identified clusters then determines the sparsity level used in the second stage of the algorithm, where multi-band splicing is performed using OMP.

3.1.2 Stage II: Multi-band splicing

The second stage of the mmSplicer algorithm performs sparse recovery to reconstruct the wideband CIR by merging measurements from several narrow bands. Multi-band splicing enhances delay resolution by effectively increasing the measurement bandwidth. For a single band, the delay resolution is given by$(\Delta\tau)_1 = 1/Nf_s$, where: N - the number of the subcarriers and f_s - subcarrier spacing. When measurements are taken across M frequencies bands the resolution is improved to $(\Delta\tau)_1 = 1/MNf_s$. Considering that the CIR is sparse, we adopt a compressed sensing approach similar to [14], using OMP to recover the CIR over the aggregated bandwidth. The OMP signal can be represented in the following form [14]:

$$\tilde{\mathbf{y}} \approx \mathbf{D}\mathbf{h}_0 + \tilde{\mathbf{z}} \tag{1}$$

where

1) $\tilde{\mathbf{y}}$ is a vector containing the CFR samples for all the bands, $\tilde{\mathbf{y}} = [\tilde{\mathbf{y}}(1)^T, ..., \tilde{\mathbf{y}}(M)^T]^T \in \mathbb{C}^{MN}$. In the case when only a set of sub-channels are used, then the rest of the entries are defined as zero.
2) a uniform grid of size G is defined over the delay domain as $\mathcal{G} = \{0, 1/G, ..., G-1/G\}/f_s$, and a dictionary $\mathbf{D}$ as $\mathbf{D} = [\mathbf{d}(0), ..., \mathbf{d}(G-1)] \in \mathbb{C}^{MN\times G}$, where $G = MN$ and each column $\mathbf{d}(i) \in \mathbb{C}^{MN}$ given as

$$\mathbf{d}(i) = \frac{1}{\sqrt{MN}}[e^{-j2\pi[\mathbf{f}]_1(\frac{i}{G})/f_s}, ..., e^{-j2\pi[\mathbf{f}]_{MN}(\frac{i}{G})/f_s}]^T, \tag{2}$$

where $i = 0, 1, ..., G-1$.
3) $\tilde{\mathbf{z}}_i$ represents the additive white Gaussian noise (AWGN)
4) $\mathbf{h}_0 \in \mathbb{C}^G$ is the estimated CIR using the OMP sparse recovery method and the given $\tilde{\mathbf{y}}$ samples.

The OMP method is a greedy iterative algorithm, that selects a column of the dictionary $\mathbf{D}$, at each iteration, such that it has the highest correlation with the current residual and it repeats until a convergence condition is met. For each selected column, the non-zero coefficients are computed using the least-square method, such that they approximate the measurement vector $\tilde{\mathbf{y}}$. This step defines the matching part of the OMP algorithm. The effect of each selected column has to be removed from the residual, such that it can not be selected again, and this defines the orthogonality of the OMP method [57]. The algorithm terminates once the number of the selected dictionary columns reaches the sparsity order of $\mathbf{h}_0$, which is given as input. In our context, the sparsity order is defined as the number of clusters identified after the 90th percentile in the first stage. Since the precise number of multipaths is typically unknown, we utilize the count from the first stage as a reference to estimate additional paths within the clusters that are indistinguishable in the narrow-band signal due to the low time-domain resolution.

3.2 Net-SpaRSA

Net-SpaRSA is an adaptation of the SpaRSA algorithm presented in [43], which is developed to solve sparse signal recovery problems[2]. Leveraging the sparse nature of the CIR, meaning only a few components are significantly nonzero, we apply Net-SpaRSA to reconstruct high-resolution CIR from narrowband measurements (cf. Figure 1). The approach is applicable to problems containing complex data, which is very relevant to our application. In its standard form, the algorithm solves optimization problems as follows:

$$\min_{\mathbf{x}} \frac{1}{2}||\mathbf{y} - \mathbf{A}\mathbf{x}||_2^2 + \lambda||\mathbf{x}||_1 \tag{3}$$

where:

- $\mathbf{x}$ is the sparse CIR to be recovered,
- $\mathbf{A}$ is the sensing matrix, containing Fourier coefficients,
- $\mathbf{y}$ is the estimated CFR from the received signal,
- $||\cdot||_2$ denotes the ℓ_2-norm (Euclidean norm),
- $||\cdot||_1$ denotes the ℓ_1-norm (absolute value norm),
- λ is a regularization parameter controlling the trade-off between data fidelity and sparsity.

Unlike Net-SpaRSA, both OMP [14], [37] and the two-stage multi-band splicing algorithm [28] do not use an optimization formulation. Net-SpaRSA follows an iterative approach, with each iteration involving an optimization subproblem consisting of a quadratic term with a diagonal Hessian and a sparsity-inducing regularizer. The algorithm terminates once a stopping criterion convergence, and a final de-biasing post-processing step adjusts the solution, counteracting any magnitude attenuation from the regularization. The diagram of the algorithm according to [43], is given in Figure 5.

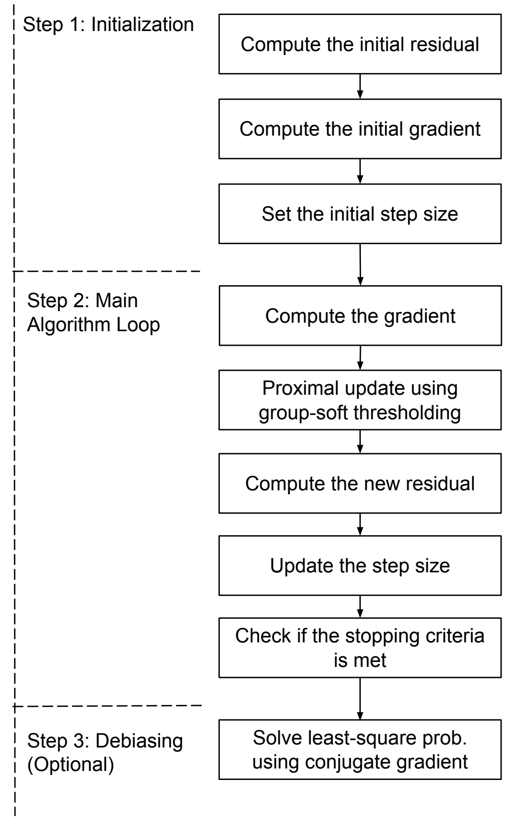

Figure 5. Block diagram of the Net-SpaRSA algorithm [43].

In summary, the selected sparse recovery algorithms are all grid-based and have been frequently chosen in the literature due to their proven effectiveness. Sparse recovery algorithms can be broadly categorized into grid-based and

[2]www.lx.it.pt/ mtf/SpaRSA

grid-less methods [59]. Grid-based algorithms discretize the parameter space into a finite grid, assuming that the parameters will approximately lie on the grid. This group of algorithms is characterized by simplicity in implementation and computational efficiency. However, the true parameters might not lie exactly on the defined grid, leading to mismatches and reduced accuracy. On the other hand, grid-less sparse methods operate in a continuous parameter space, avoiding discretization, which results in higher accuracy, particularly in high-resolution applications. Nevertheless, grid-less methods typically require higher computational complexity and pose greater challenges in implementation. In this work, we focus only on grid-based methods due to their low computational complexity, and we consider the evaluation of grid-less algorithms as future work.

The widely used OMP algorithm is well-known for its simplicity, making it easy to implement and computationally feasible for real-time or near-real-time applications. However, OMP is also sensitive to noise, which can lead to incorrect solutions.

In contrast, the Net-SpaRSA algorithm, is optimization-based and performs sparse recovery by minimizing a ℓ_1-regularized objective function. It does not require an explicit sparsity level, instead, the trade-off between sparsity and reconstruction accuracy is controlled via a regularization parameter. While effective in producing globally sparse solutions, SpaRSA does not incorporate prior information about the likely positions of MPCs. This approach tends to be robust to noise and achieves higher accuracy. Nonetheless, the iterative nature of this optimization makes it computationally expensive, particularly for large-scale CFR data.

Finally, our mmSplicer algorithm is designed as a two-stage enhancement of the standard OMP to improve its performance in the context of multiband channel splicing. The first stage leverages a single narrowband CFR to estimate the locations of the dominant MPCs by transforming it to the time domain, applying thresholding, and grouping peaks into clusters. The number of clusters determines the sparsity level, which is then used to initialize OMP in the second stage. This targeted use of prior information allows mmSplicer to focus the reconstruction on time intervals where MPCs are most likely to occur, increasing robustness while maintaining low computational complexity.

4 System Setup

In the following, we describe the system architecture and the estimation technique used for generating the CIR and CFR. The SDR-based channel sounder builds upon USRP-components (i.e., X310, with an ADC resolution of 14 bits) to perform the over-the-air communication, and MATLAB for the software implementation (cf. Figure 1(b)).

The OFDM transmitter is implemented according to the 802.11ac standard, which supports the signal bandwidths of 20, 40, 80 and 160 MHz. Over the different signal bandwidths, the OFDM subcarrier spacing is kept fixed to 312.5 kHz, whereas the number of the subcarriers changes accordingly, following the standard. We conduct over-the air-experiments both at sub-6 GHz and 60 GHz. To up-convert and transmit the signal at 60 GHz, we use the sivers

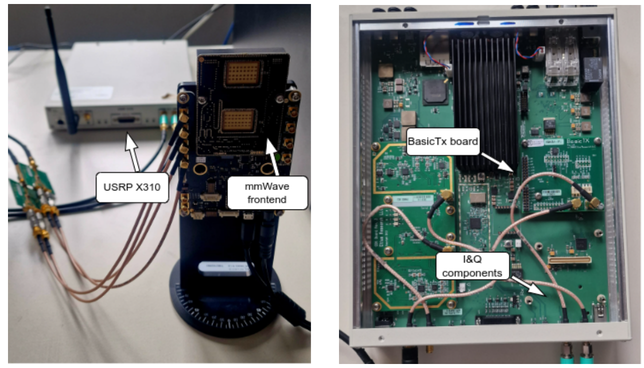

(a) Phased array antenna and USRP X310.

(b) Basic TX board inside the USRP X310 for splitting the signal into I/Q components.

Figure 6. Lab setup: Phased array antennas connected to USRP X310 using the BasicTx board.

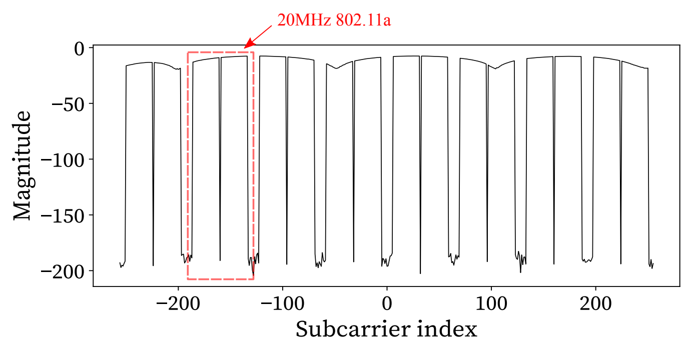

Figure 7. Illustration of the recurring pattern in the 160 MHz L-LTF of the 802.11ac frame.

semiconducter phase array antennas[3], which are connected to the USRPs through the BasicTX/BasicRX boards (cf. Figure 6). We utilize MATLAB to generate and post-process the data, and UHD drivers to transmit and receive the signal.

The captured signal is down-converted, and the raw data is stored into a binary file for further post-processing on the host computer. During post-processing, the time and carrier frequency offset are estimated and compensated per each received packet. The channel is estimated using the LS estimation technique, and the obtained CIR and CFR are stored into files. The estimation is performed using either the very high throughput long training field (VHT-LTF) or the legacy long training field (L-LTF). Finally, the signal is decoded and demodulated, and the transmitted payload message is recovered. The collected CFR samples over multiple narrow frequency bands are used as input to the spectrum splicing technique for estimating the wideband channel.

For the rest of the paper, the estimation is performed on the L-LTF. This field is characterized by a repetitive pattern of the IEEE 802.11a long training field (LTF). For instance, as depicted in Figure 7, the 802.11ac 160 MHz L-LTF is comprised of eighth repetitive copies of the 20 MHz IEEE 802.11a LTF. The plot shows the magnitude (in db) for each subcarrier, where the subcarriers with the lowest magnitude are the null subcarriers. This characteristic is leveraged to emulate the L-LTF of narrow-band signals within the wider

[3]https://www.sivers-semiconductors.com/sivers-wireless/wireless-products/evaluation-kits/

160 MHz L-LTF, which is subsequently utilized in algorithm validation within the paper, temporarily disregarding the issue of hardware distortions.

Channel estimation is performed using LS estimation time or frequency domain approach [45]. The time-domain approach computes the CIR as

$$\hat{h} = X^{\dagger}y, \tag{4}$$

where y are the received samples, $\hat{h}$ is the CIR and $X^{\dagger}$ is the Moore-Penrose (pseudo) inverse of the Toeplitz matrix X. Likewise, the frequency-domain approach acquires the CFR as

$$\hat{H}[k] = \frac{Y[k]}{X[k]}, \tag{5}$$

where $Y[k]$ denotes the received symbols at subcarrier k, $\hat{H}[k]$ is the estimated CFR at subcarrier k, and $X[k]$ are the transmitted symbols at subcarrier k. Both CIR and CFR can be computed from each other using the fast Fourier transformation (FFT) and inverse FFT (IFFT).

5 Going beyond Theory: Practical Channel Splicing for OFDM Systems

Multi-band splicing concatenates the CFR samples obtained from narrow-band measurements taken across multiple frequency bands. This approach increases the effective bandwidth and, consequently, the time-domain resolution. Over the years, various algorithms have been developed, becoming even more complex but leading to more accurate results. We specifically focus on multi-band splicing using compressed sensing, which offers a significant advantage by allowing the estimation of a wide channel from samples collected over just a few frequency bands. This reduction in the number of required measurements is essential for addressing the challenges posed by channel coherence time in the mmWave frequency band. We concentrate on two well-known grid-based sparse recovery algorithms, along with an extended method, and compare their performance in a controlled simulated environment, in an ideal case (using wires) and real-world scenarios, exploiting the flexibility of the developed tool to switch between theory and practice. This step is crucial for gaining insights into the behavior of the algorithms when integrated into a real communication system, enabling us to identify both their strengths and weaknesses.

To validate the models, we leverage the repetitive pattern of the L-LTF in the 802.11ac standard, to replicate $8 \times 20\,\mathrm{MHz}$ narrow-band channels within wide-band signals. An illustration of the experimental procedure is presented in Figure 8. This approach effectively mimics the concept of multi-band splicing, under the assumption that the input data is free from hardware-induced distortions. In this way, we neglect at the moment the issue of the hardware distortions, as our primary focus is on validating the models. However, addressing these distortions remains a crucial step before combining narrowband measurements at different center frequencies, which we will investigate in future work. For all algorithms, we set the grid size to $G = 1MN$. While many existing algorithms [59] have verified that a dense grid ($G \gg MN$) can enhance estimation accuracy by mitigating grid mismatch, this benefit does not apply in our specific measurement setup. Since our system has a total bandwidth of $BW = 1MN$, the time resolution $1/MN$. As a result, the multipath components can only be distinguished at discrete time instances separated by $1/MN$. Increasing the grid density beyond $G = 1MN$ (e.g., $G = 2MN$, or $G = 3MN$) would introduce additional dictionary elements that do not correspond to actual multipath delays, thereby increasing computational complexity without improving accuracy.

In order to fairly compare the algorithms, we make the following assumptions:

- *OMP algorithm*: The stopping condition is set equal to the total number of the subcarriers of the 160 MHz signal (i.e., 512).
- *mmSplicer*: The number of clusters in the first stage in set equal to the number of the subcarriers of the narrow-band signal 20 MHz (i.e., 64).
- *Net-SpaRSA*: The regularization parameter λ, is set to 0.

We executed the algorithms on $4 \times 20\,\mathrm{MHz}$ sub-bands (from a total of $8 \times 20\,\mathrm{MHz}$) exploring the following sub-band distributions: A. all available sub-bands are consecutive; B. the available sub-bands are non-consecutive, but the gaps in between are small, i.e., 40 MHz; C. the available sub-bands are widely spaced, with 80 MHz gap in between. These configurations are illustrated in Step 3 in Figure 8.. This approach allows us to analyze the impact of sub-band positioning on performance. The splicing techniques were applied across 40 packets. A slight amplitude variation is noticeable across the packets due to clock synchronization issues between the transmitter and receiver. For each method, we present the range of magnitudes, including the average (marked), minimum, and maximum values. Each plot illustrates the amplitude range across all packets of the reference 160 MHz signal alongside the estimated magnitude ranges for different configurations (Step 5 in Figure 8). It is important to note that the true channel is not directly observable under experimental conditions, particularly due to its time-varying nature. In this paper, we define the "reference" as a snapshot of the CIR estimated using a 160 MHz signal in different scenarios. This snapshot serves as a baseline for comparison throughout our analysis. To enhance clarity, only the initial sets of taps are displayed, with results for each configuration slightly offset to prevent overlap and improve visibility.

5.1 Simulations

Firstly, we present the numerical outcomes obtained from our simulations, wherein the algorithms undergo validation at a center frequency of 5 GHz, utilizing a 160 MHz signal. Signal up/down-conversion is implemented in MATLAB, and the real communication channel is model using the Rayleigh channel. This channel model allows defining the number of the MPCs and the time delay for each path. Our objective is to validate the algorithms under conditions wherein the MPCs are closely spaced, making them indistinguishable from narrow band signals. To achieve this, we construct a scenario comprising of $K = 2$ MPCs, with delays set at $\{0, 6.25\}\mathrm{ns}$. The channel estimation at the receiver is performed using the LS estimation techniques, utilizing the

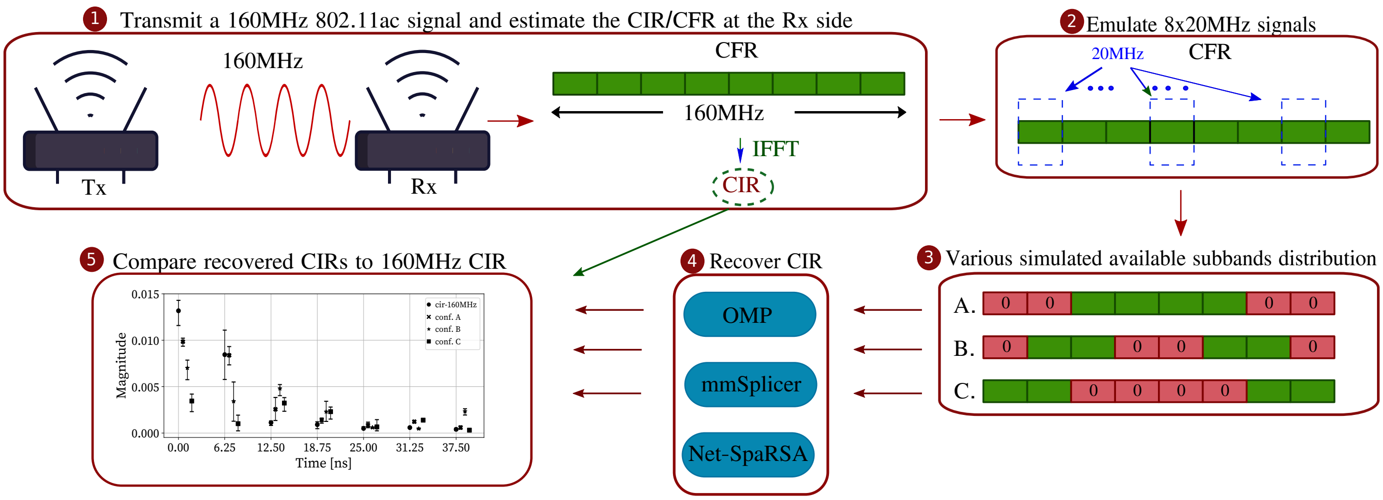

Figure 8. Illustration of the experimental procedure.

L-LTF, characterized by a recurring pattern (802.11a LTF). We exploit this advantage, and emulate 8×20 MHz narrow-band signals. Subsequently, the algorithms are executed over half of these sub-bands, and the resultant estimates are compared against the 160 MHz CIR, which serves as reference or baseline. Employing a sub-set of the 20 MHz bands offers the flexibility in exploring the impact of different sub-band placements. Specifically, we examine the following three configurations: A. all available sub-bands are consecutive (conf. A); B. the available sub-bands are non-consecutive, but the gaps in between are small, i.e., 40 MHz (conf. B); C. the available sub-bands are widely spaced, with 80 MHz gap in between (conf. C); as illustrated in Step 3 in Figure 8.

The results for the three algorithms across these configurations are depicted in Figure 9. Each tap's magnitude range (maximum and minimum values) over 40 packets, alongside the average value, is showcased. However, since simulations are not affected by hardware distortions, there are no magnitude variations across packets. Additionally, the plots include the 160 MHz CIR, illustrating the presence of two strong paths: the LoS and the second component at 6.25 ns, as defined in the Rayleigh channel model.

Generally, all the algorithms have the tendency to under-estimate the strong MPCs and over-estimate the low-energy spikes. This trend is expected since a decrease in the number of observations results in a smoothing effect, where strong MPCs are underestimated, while weaker ones are overestimated to maintain consistency. Surprisingly, mmSplicer and Net-SpaRSA algorithms yield very similar results, with negligible difference. Both methods, estimate a weaker CIR compared to the reference reference one but exhibit the same pattern. In contrast, OMP generates a wide range of amplitudes for each tap. Due to the very large stopping condition value, occasionally the algorithm estimates multiple magnitude values for the same tap some of which may be close to zero. This behavior is not observed in the mmSplicer outcomes, despite the fact that the method is based on OMP, as the stopping condition is significantly lower.

Regarding sub-band space, mmSplicer and Net-SpaRSA algorithms exhibit optimal performance in terms of the average values with consecutive bands (conf. A), closely aligning

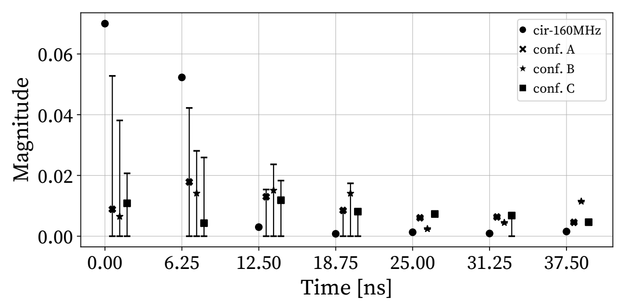

(a) OMP estimation results.

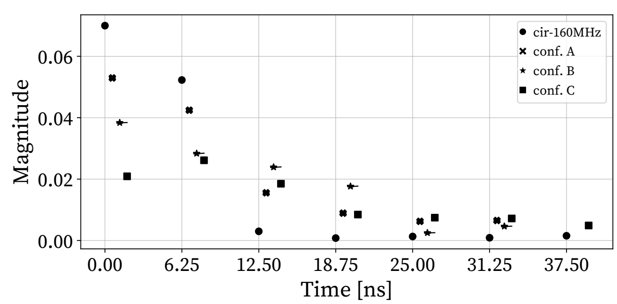

(b) mmSplicer estimation results.

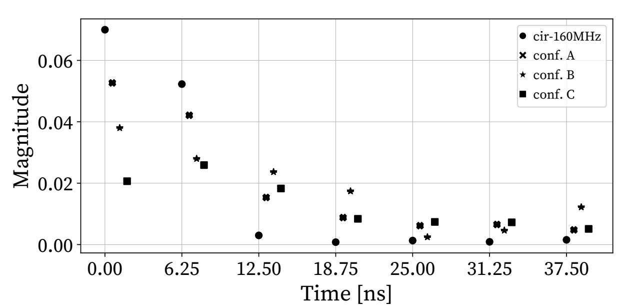

(c) Net-SpaRSA estimation results

Figure 9. Validation using simulation. Markers show the average values, together with the variance.

with the reference 160 MHz CIR. Performance deteriorates as the spacing between sub-bands increases (particularly to 80 MHz) (conf. C), making it more challenging to distinguish the two strong paths. In the case of OMP, due to the algorithm performance, the maximum value proves to be a better indicator for distinguishing strong paths. Once again, the consecutive bands configuration (conf. A) yields superior outcomes.

5.2 Cable Experiments

We now study the performance of the multi-band splicing techniques under an ideal scenario by emulating multipath components utilizing RF splitters, combiners, and coaxial cables. The RF splitter is connected to the output port of the USRP X310 transmitter and splits the output signal into two copies, which go through different cable lengths (multipath components). On the other side, the RF combiner combines the two signals coming from the two paths, and it is connected to the input port of the USRP X310 receiver. The cable lengths are 2 m and 10 m respectively. The speed of the RF signal in the coaxial cable depend on the dielectric constant, typically ranging between 66% to 85% of the speed of light in the vacuum. We transmit a 160 MHz signal which translates to a resolutions of 6.25 ns. To validate the algorithms we estimate the CFR using the L-LTF in the 802.11ac frame. Exploiting the pattern of the L-LTF, which consists of multiple copies of the 802.11a legacy preamble, we emulate in it 8×20 MHz signal legacy preamble. As the resolution of a single 20 MHz signal is 50 ns, it cannot distinguish the two paths.

The outcome from each algorithm are depicted in Figure 10. The 160 MHz CIR reveals two strong MPCs (the LoS path and the reflection at 31.25 ns). Additional low energy spikes in between the two MPCs might be a consequence of hardware components.

A common pattern across all algorithms is the underestimation of the two strong MPCs and the overestimation of low-energy spikes. This behavior aligns with the expected smoothing effect, where a reduced number of observations causes stronger MPCs to appear weaker, while weaker components are amplified to preserve overall consistency. Interestingly, the two-stage and Net-SpaRSA algorithms yield very similar results, with negligible differences in estimated magnitude changes. In contrast, the performance of the OMP algorithm with respect to the average value is inferior, displaying a larger range of magnitude values. This behavior can be attributed to the large stopping condition value, leading the method to estimate magnitude values close to zero (or zero).

In terms of different sub-bands distributions, drawing clear conclusion presents a challenge. Overall, a sub-band space of 80 MHz (conf. C) results in weak CIR estimation, making it very difficult to distinguish the strong paths. Looking at the average value, the consecutive bands (conf. A) and 40 MHz apart bands (conf. B) yield relatively to better results. The total estimated CIR is weaker in these cases, but a similar pattern to the reference CIR can still be observed. This observation does not hold for the OMP method, where focusing on the maximum value of consecutive bands can lead to better results.

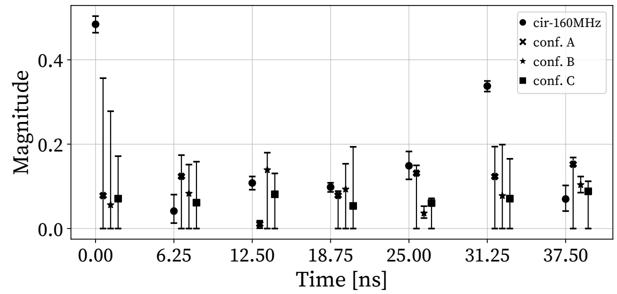

(a) OMP estimation results.

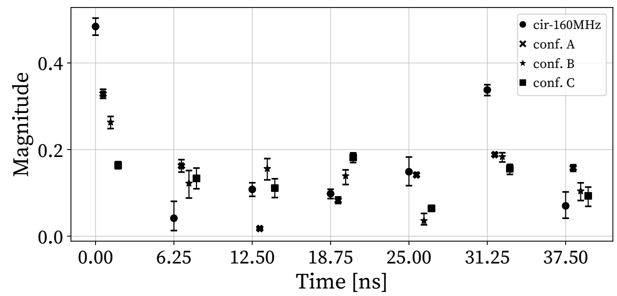

(b) mmSplicer estimation results.

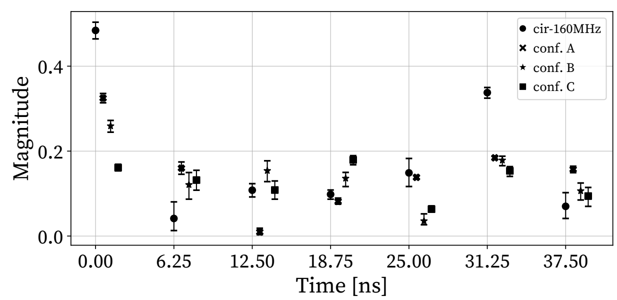

(c) Net-SpaRSA estimation results

Figure 10. Cable experiments. Markers show the average values, together with the variance.

5.3 Sub-6GHz Indoor Lab-Experiments

After validating the algorithms in an ideal scenario consisting of cables emulating the multipath components, we start conducting measurements in real-world at the 2.4 GHz frequency. These experiments were conducted indoor using a 160 MHz signal at a communication distance of 7.5 m. The 160 MHz bandwidth resolution enables differentiating paths coming relatively close, to a distance difference of 1.8 m. Considering the signal propagation characteristics at 2.4 GHz and the crowded indoor environment were the measurements were conducted, we anticipated a CIR with multiple strong paths. Similar to the previous experiments, the channel is estimated based on the L-LTF, and 8×20 MHz narrow-band signals are emulated to analyze the performance of the considered algorithms.

The full 160 MHz estimated CIR and the algorithms outcomes are presented in Figure 11. The plots illustrate the range of amplitudes across 40 packets for each configuration and tap, showing the reference CIR and estimated values, along with the average (with markers), minimum, and maximum values. As expected, the 160 MHz CIR shows the presence of several spikes in the proximity of each other (LoS and 6.25 ns; 18.75 ns, 25 ns, and 31.25 ns).

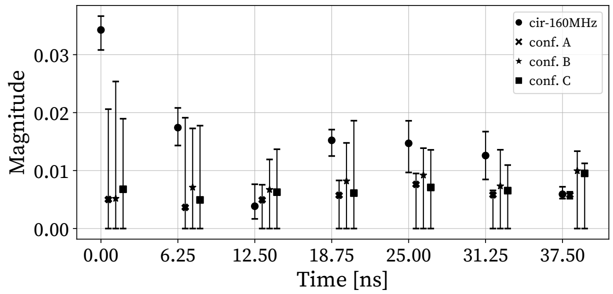

(a) OMP estimation results.

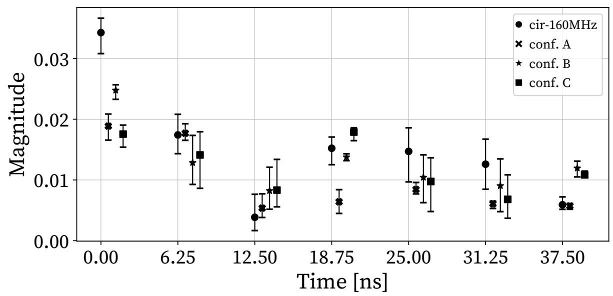

(b) mmSplicer estimation results.

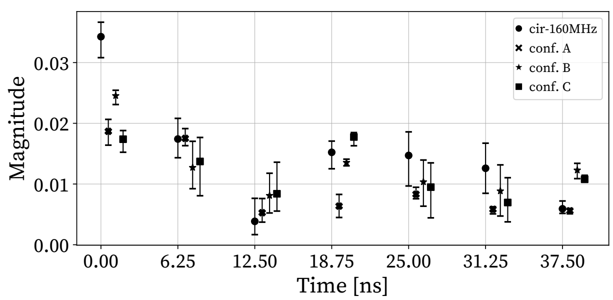

(c) Net-SpaRSA estimation results

Figure 11. Sub-6GHz indoor lab-experiments. Markers show the average values, together with the variance.

Overall, the algorithms tend to underestimate the strong spikes and overestimate the low-energy ones, which aligns with the expected smoothing effect that occurs when the number of observations decreases, causing stronger MPCs to be underestimated while weaker ones are overestimated to maintain consistency. The mmSplicer and Net-SpaRSA generate very similar results, with a very slight negligible difference in amplitude. Both algorithms follow the same CIR pattern as the reference 160 MHz CIR. In contrast the range of the amplitudes estimated by OMP is very wide, leading to difficulty in distinguishing the strong paths when looking at the average values. This is a consequence of the very large stopping condition, resulting sometimes in estimated values close to zero for each tap.

Next we focus on analyzing performance across different sub-band spacing. Drawing conclusions in such scenario with multiple spikes proved to be more challenging. While various configurations tended to approximate better the pattern and values of different paths, we can still see that results obtained from the sub-bands spaced 80 MHz (conf. C) are the ones furthest from the baseline, in terms of the average value, and the maximum value for the OMP.

6 Channel Splicing in Action at mmWave Frequencies

After validating the sparse recovery algorithms in the context of multi-band splicing, our focus now shifts to the mmWave frequency band – in the scope of this paper, we specifically use the 60 GHz ISM band. Measurements were conducted in the laboratory at a distance of 7.5 m, employing the Sivers Semiconductors phased array antennas and specifically, the BFM06009 module consisting of a 8x2x2 antenna array, supporting steering both in elevation and azimuth. Given the phased array antenna's narrow beam width (about 10°), to facilitate testing the algorithms two mirrors were added to the setup. The first mirror is positioned behind the receiver antenna, while the second one was placed in the proximity of the communication link, approximately 1.5 m from the receiver.

Following a similar methodology as in previous scenarios, a 160 MHz signal is transmitted over the air, and the channel is estimated at the receiver using the LS estimation technique and the L-LTF. Exploiting the repetitive nature of the L-LTF, 8×20 MHz signals are emulated and the algorithms were executed for different sub-band spacing as illustrated in Figure 8. The results of the algorithms are presented in Figure 12, depicting the range of the magnitudes along with the average (represented by markers), minimum and maximum values, for the reference (160 MHz CIR) and the estimated results. The 160 MHz CIR shows the present of two strong MPCs: the LoS path and the component at 6.25 ns. In contrast to previous scenarios, the range of the amplitude values for these two strong paths is slightly larger, indicating that the 60 GHz channel is more sensitive to small changes in the environment.

Across the sparse recovery algorithms, the two strong MPCs tend to be underestimated, while the low-energy spikes are overestimated, which aligns with the expected smoothing effect that occurs when the number of observations decreases, causing stronger MPCs to be underestimated and weaker ones to be overestimated in order to maintain consistency. Similar to the previous scenarios, the mmSplicer and Net-SpaRSA algorithms yields to very similar results with a negligible difference in the estimated amplitudes. Both algorithms accurately capture the CIR pattern observed in the reference one, especially when consecutive bands (conf. A) or sub-bands spaced 40 MHz (conf. B) were utilized. The performance degrades as the spacing between sub-bands increases, emphasising the influence of band selection on the generated outcomes. Regarding the OMP algorithm, it struggles to capture the CIR pattern, irrespective of the selected sub-bands. This comes as a consequence of the very large stopping condition used, which deteriorates the algorithm performance.

7 Complexity

Multi-band splicing is a powerful technique that has recently gained significant attention in extending the communication systems to support sensing applications. This method allows for the use of existing hardware to perform extensive channel measurements efficiently. While a few channel splicing approaches have already been developed, they are either known for their computational complexity

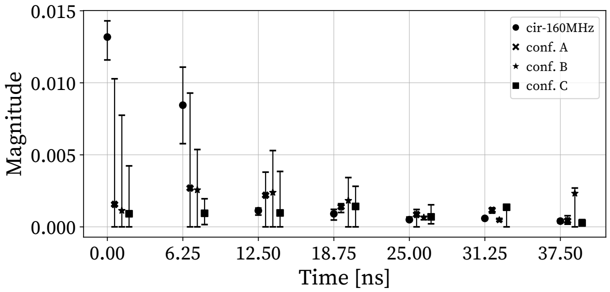

(a) OMP estimation results.

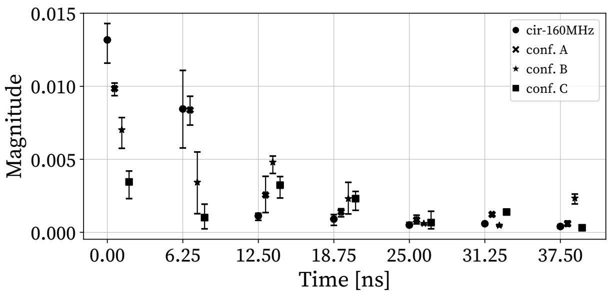

(b) mmSplicer estimation results.

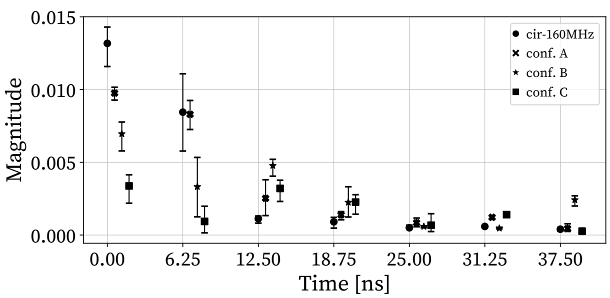

(c) Net-SpaRSA estimation results

Figure 12. mmWave channel splicing at 60 GHz. Markers show the average values, together with the variance.

or for low accuracy. We contribute to the field with two approaches: (1) we extended the OMP-based multi-band splicing technique [14] to a two-stage algorithm, called mmSplicer, and (2) we tuned the SpaRSA algorithm [43] to work in a communications scenario, resulting in Net-SpaRSA. In this section, we focus on comparing these algorithms in terms of their computational complexity and their system-dependent execution time, abstracting away hardware and implementation details. Analyzing complexity is crucial due to the impact of channel coherence time on performance.

7.1 Execution Time

The first parameter we consider when comparing the complexity of the algorithms is the execution time. Execution time refers to the total duration required for a computer to execute an algorithm, typically measured in seconds [60]. It depends on several factors, including the algorithm design, implementation efficiency, input data size, and most importantly, the hardware specifications of the system, such as CPU speed, memory, and system load at the time of execution. As a result, the execution time varies depending on the computing environment and external system conditions. We measured the execution time of the three algorithms using a system with the following specifications: AMD Ryzen 9 7950X 16-Core processor and 128 GB RAM.

Table 1
Average execution time and standard error of OMP, Net-SpaRSA, and mmSplicer across different scenarios.

Frequency	OMP (s)	Net-SpaRSA (s)	mmSplicer (s)
simulations	3.595 ± 0.001026	0.124 ± 0.000013	0.234 ± 0.000184
cable 5 GHz	3.692 ± 0.002139	0.123 ± 0.000012	0.235 ± 0.000060
2.4 GHz	3.690 ± 0.002489	0.122 ± 0.000037	0.260 ± 0.000210
60 GHz	3.699 ± 0.002190	0.127 ± 0.000027	0.231 ± 0.000060

To compute execution time in MATLAB we utilized the built-in *tic* and *toc* functions. The *tic* function records the current time, while *toc* returns the elapsed time since the last tic call. However, as stated in the MATLAB documentation, if an algorithm's execution time is less than 0.1 s, the precision of *tic* and *toc* may be insufficient. To ensure reliable execution time measurements, each algorithm was executed 100 times in a loop, and the total elapsed time was recorded and divided by 100. This procedure was repeated 1,000 times and the average execution time was computed across these runs in order to compensate for random fluctuations. The algorithms were executed for each scenario while maintaining the same system configuration (conf. A: all available sub-bands are consecutive, as shown in Figure 8), ensuring that the input data size remained consistent across all runs. Furthermore, the execution time was evaluated under the same conditions as the experimental process. Specifically, the number of iterations in the OMP algorithm was set equal to the number of subcarriers in the 160 MHz signal, while for the mmSplicer algorithm, it was set to the number of subcarriers in the narrowband signal (i.e., 64 subcarriers). Additionally, the regularization parameter of the Net-SpaRSA algorithm was set to 0.

The final results are presented in Table 1, where each entry includes the mean execution time along with the standard error of the mean to quantify the measurement uncertainty. The results show that, under the given conditions, the Net-SpaRSA algorithm has the shortest execution time, followed by the mmSplicer algorithm, and then the OMP algorithm. However, it is important to note that the assumed condition for the OMP algorithm represents the worst-case scenario. In practice, the number of iterations would be significantly lower, given the sparsity of the CIR.

As mentioned earlier, execution time refers to the total wall-clock time required for a computer to execute an algorithm. It depends on various factors, including implementation efficiency and, most notably, the system's hardware specifications. Therefore, in addition to the execution time, we also analyze the computational complexity of the algorithms to provide a system-independent measure of their performance.

7.2 Computational Complexity

The computational complexity of an algorithm describes how its execution time scales with the input size, typically expressed in Big O notation. This notation characterizes the worst-case performance of an algorithm, abstracting hardware and implementation details [61]. We analyze the computational complexity of our three algorithms based on the key operations performed during execution, particularly matrix-vector multiplications and iterative updates.

OMP: The time complexity of the OMP algorithm depends on the number of iterations K, which corresponds to the sparsity level of the recovered signal. In each iteration, the algorithm first computes the inner product between the residual (of size $1 \times MN$ in our case) and all dictionary columns to identify the column most correlated with the residual. This involves a matrix-vector multiplication with a complexity of $\mathcal{O}(M^2N^2)$. Once the most correlated column is selected, an operation with complexity $\mathcal{O}(MN)$, the nonzero coefficients are computed using the least squares method. This requires solving a $K \times K$ system of equations, which has a complexity of $\mathcal{O}(K^3)$ per iteration. Finally, the residual is updated, requiring a matrix-vector multiplication with complexity $\mathcal{O}(MN)$. Summing these operations over K iterations and keeping only the dominant terms, the total complexity of OMP is given as

$$\mathcal{O}(KM^2N^2 + K^4) \tag{5}$$

Net-SpaRSA: The complexity of Net-SpaRSA depends on the number of iterations required for convergence. The initialization phase, which includes the initial computation of the residual and gradient, consists of a matrix-vector multiplication with complexity $\mathcal{O}(M^2N^2)$. The algorithm's main loop then runs until it converges to a solution. In each iteration, the soft thresholding operation is applied element-wise with complexity $\mathcal{O}(MN)$, and the gradient update involves a matrix-vector multiplication with complexity $\mathcal{O}(M^2N^2)$. Considering K number of iterations, the total complexity is $\mathcal{O}(KM^2N^2)$ The debiasing phase employs the conjugate gradient method to solve the least squares problem iteratively, where each iteration involves a matrix-vector multiplication with complexity $\mathcal{O}(KMN)$, leading to an overall complexity of $\mathcal{O}(K^2MN)$ over K iterations. Thus, the total complexity of the Net-SpaRSA algorithm is given as

$$\mathcal{O}(K^2MN + KM^2N^2) \tag{6}$$

mmSplicer: The mmSplicer algorithm extends the OMP method by introducing an additional stage to automatically determine the number of iterations K, which is required for the second stage where OMP is applied. In the first stage, the algorithm takes as input the CFR samples from a single narrowband measurement ($1 \times N$ size). The IFFT is then applied to obtain the CIR, which has a computational complexity of $\mathcal{O}(NlogN)$. Next, the magnitude values are computed by taking the absolute value, and sorted, with a threshold set at the 90th percentile. The sorting operation has a complexity of $\mathcal{O}(NlogN)$. Finally, nearby magnitude values exceeding the threshold are grouped into clusters. The number of clusters determines the sparsity level K for the subsequent OMP step, and this clustering process has a complexity of $\mathcal{O}(N)$. Combining both stages, the total complexity of the mmSplicer algorithm is given as

$$\mathcal{O}(NlogN + KM^2N^2 + K^4) \tag{7}$$

Table 2
Computational complexity of OMP, mmSplicer, and Net-SpaRSA.

Algorithm	Complexity
OMP	$\mathcal{O}(KM^2N^2 + K^4)$
mmSplicer	$\mathcal{O}(NlogN + KM^2N^2 + K^4)$
Net-SpaRSA	$\mathcal{O}(K^2MN + KM^2N^2)$

Table 2 presents the time complexity of the three algorithms, indicating that OMP is the most efficient. The mmSplicer algorithm, which includes an additional preprocessing step, is slightly more computationally expensive than OMP but remains more efficient than Net-SpaRSA. Net-SpaRSA has the highest complexity due to its iterative updates in both the main loop and the debiasing phase.

Given the above, a trade-off must be made between algorithm performance and complexity. Indeed, mmSplicer adds an additional stage on top of the classical low-complexity OMP algorithm, thereby increasing the complexity. However, this first stage enables mmSplicer to automatically determine the required number of iterations for the second stage to recover the CIR. In contrast, pure OMP requires the user to specify the number of iterations as input—a requirement that is impractical in real-world scenarios, where this information is not available beforehand. Compared to Net-SpaRSA, mmSplicer achieves similar performance but with lower overall complexity.

8 Discussion

We explored three grid-based sparse recovery methods: the standard OMP algorithm, along with our two new contributions: mmSplicer, which extends OMP into a two-stage approach to enhance its applicability in wireless systems, and Net-SpaRSA, an adaptation of the SpaRSA algorithm for wireless applications. These algorithms were integrated into an experimental setup using SDRs in our lab. Specifically, they were embedded in an IEEE 802.11ac-based communication system, with CIR and CFR estimated using the LS estimation technique.

A series of lab experiments were conducted to demonstrate the feasibility of spectrum splicing in real-world environments. We focused particularly on the ability to obtain wideband channel properties using only a subset of sub-bands. This is significant, especially when considering the issue of coherence time in mmWave systems and the influence of spectrum load from other applications or users sharing the same spectrum. Both simulations and indoor experiments yielded highly accurate estimations of multipath components, particularly in terms of time delay. In terms of magnitude, we observed a common trend across all sparse recovery algorithms: strong MPCs tended to be underestimated, while low-energy components were overestimated. This effect aligns with the expected smoothing behavior that occurs when the number of observations decreases, causing stronger MPCs to appear weaker and weaker MPCs to appear stronger to maintain overall consistency. Nevertheless, for sensing applications, exact magnitude reconstruction may not be as critical as accurate path detection. As long as strong MPCs are correctly identified as such, and no negligible component is misclassified as a strong path, the algorithms remain effective for path detection tasks. Overall the results depict that the two-stage mmSplicer and Net-SpaRSA algorithms produce nearly identical results, with negligible magnitude differences. In contrast, OMP performs worse on average, showing a wider magnitude range due to its high stopping condition, which leads to estimates near or at zero.

Additionally, we analyzed the execution time and computational complexity of the algorithms, as these are critical factors when comparing different approaches. Our results showed that mmSplicer and Net-SpaRSA produced very similar results in terms of recovering the CIR, regardless of the scenario or sub-band distribution. When it came to execution time, Net-SpaRSA proved to be faster. However, it is essential to note that the assumptions made for the OMP algorithm and mmSplicer represent the worst-case scenario. In practice, the number of iterations is expected to be much lower, since the signal is sparse, especially in mmWave frequency bands. Moreover, execution time is heavily dependent on hardware and implementation; for example, the algorithms' execution time could be further optimized for real-time systems by using FPGA or C++ implementations. On the other hand, while Net-SpaRSA showed faster execution, it is computationally more complex due to the presence of iterations in both the main loop and the debiasing process. OMP, on the other hand, has the lowest computational complexity but requires the channel sparsity to be input as a parameter, which is not known beforehand.

This makes mmSplicer the best trade-off, as it offers a balance between execution time and computational complexity while not relying on prior knowledge of channel sparsity.

9 Conclusion

Following the key concepts of joint communication and sensing, we explored multi-band splicing to extend communication systems for high-accuracy sensing applications. Multi-band splicing combines multiple narrow-band measurements, taken at different (not necessarily consecutive) center frequencies, to achieve precise wideband measurements. We evaluated three grid-based sparse recovery algorithms: the standard OMP algorithm and our two novel contributions—mmSplicer, which introduces a two-stage approach to enhance OMP's applicability in wireless systems, and Net-SpaRSA, an adaptation of the SpaRSA algorithm tailored for wireless applications. Through extensive simulations and experimental validation, we assessed their performance in reconstructing wideband channel properties using only a subset of subbands with different distribution patterns. Additionally, we analyzed execution time and computational complexity to compare their practical feasibility. Overall, our findings indicate that mmSplicer provides the best trade-off between performance and complexity, offering robust multipath estimation without requiring prior knowledge of channel sparsity.

Future work will involve experiments in more dynamic scenarios to investigate how sub-bands width and spacing affect the splicing accuracy across the frequency spectrum. Additionally, we plan to explore a grid-less approach and assess its potential advantages over our existing mmSplicer algorithm in wireless scenarios. Furthermore, we aim to expand the application of multi-band splicing, currently implemented in single-input single-output (SISO) systems, to multiple-input multiple-output (MIMO) setups.

References

[1] J. Wang, N. Varshney, C. Gentile, S. Blandino, J. Chuang, and N. Golmie, "Integrated Sensing and Communication: Enabling Techniques, Applications, Tools and Datasets, Standardization, and Future Directions," *IEEE Internet of Things Journal*, Jul. 2022.

[2] J. A. Zhang, M. L. Rahman, K. Wu, X. Huang, Y. J. Guo, S. Chen, and J. Yuan, "Enabling Joint Communication and Radar Sensing in Mobile Networks - A Survey," *IEEE Communications Surveys & Tutorials*, vol. 24, no. 1, pp. 306–345, 2022.

[3] T. Wild, V. Braun, and H. Viswanathan, "Joint Design of Communication and Sensing for Beyond 5G and 6G Systems," *IEEE Access*, vol. 9, Jan. 2021.

[4] Y. Cui, F. Liu, X. Jing, and J. Mu, "Integrating Sensing and Communications for Ubiquitous IoT: Applications, Trends, and Challenges," *IEEE Network*, vol. 35, no. 5, pp. 158–167, Sep. 2021.

[5] K. Wu, J. A. Zhang, X. Huang, and Y. J. Guo, "OTFS-Based Joint Communication and Sensing for Future Industrial IoT," *IEEE Internet of Things Journal*, vol. 10, no. 3, pp. 1973–1989, Feb. 2023.

[6] S. D. Liyanaarachchi, C. B. Barneto, T. Riihonen, and M. Valkama, "Joint OFDM Waveform Design for Communications and Sensing Convergence," in *IEEE International Conference on Communications (ICC 2020)*, Virtual Conference: IEEE, Jun. 2020.

[7] X. Li, H. Wang, J. Hu, Z. Chen, Z. Jiang, and J. Luo, "CCS-Fi: Widening Wi-Fi Sensing Bandwidth via Compressive Channel Sampling," in *44th IEEE International Conference on Computer Communications (INFOCOM 2025)*, to appear, London, United Kingdom: IEEE, May 2025.

[8] D. Vasisht, S. Kumar, and D. Katabi, "Decimeter-level localization with a single WiFi access point," in *13th USENIX Symposium on Networked Systems Design and Implementation (NSDI 2016)*, Santa Clara, CA, Mar. 2016, pp. 165–178.

[9] T. Kazaz, G. J. Janssen, J. Romme, and A.-J. Van der Veen, "Delay estimation for ranging and localization using multiband channel state information," *IEEE Transactions on Wireless Communications*, vol. 21, no. 4, pp. 2591–2607, 2021.

[10] Y. Xie, Z. Li, and M. Li, "Precise Power Delay Profiling with Commodity Wi-Fi," *IEEE Transactions on Mobile Computing*, vol. 18, no. 6, pp. 1342–1355, Jun. 2019.

[11] J. Xiong, K. Sundaresan, and K. Jamieson, "Tonetrack: Leveraging frequency-agile radios for time-based indoor wireless localization," in *21st ACM International Conference on Mobile Computing and Networking (MobiCom 2015)*, Paris, France, Sep. 2015, pp. 537–549.

[12] W. Guo and L. Jing, "Toward Low-Cost Passive Motion Tracking With One Pair of Commodity Wi-Fi Devices," *IEEE Journal of Indoor and Seamless Positioning and Navigation*, vol. 1, pp. 39–52, Jun. 2023.

[13] X. Shen, L. Guo, Z. Lu, X. Wen, and Z. He, "WiRIM: Resolution improving mechanism for human sensing with commodity Wi-Fi," *IEEE Access*, vol. 7, pp. 168 357–168 370, Nov. 2019.

[14] M. B. Khalilsarai, B. Gross, S. Stefanatos, G. Wunder, and G. Caire, "WiFi-Based Channel Impulse Response Estimation and Localization via Multi-Band Splicing," in *IEEE Global Communications Conference (GLOBECOM 2020)*, Taipei, Taiwan: IEEE, Dec. 2020.

[15] Y. Wan, A. Liu, R. Du, and T. X. Han, "Fundamental Limits and Optimization of Multiband Sensing," arXiv, eess.SP, Jul. 2022.

[16] Y. Wan, A. Liu, Q. Hu, M. Zhang, and Y. Cai, "Multiband Delay Estimation for Localization Using a Two-Stage Global Estimation Scheme," arXiv, eess.SP, Jun. 2022.

[17] S. Dimce and F. Dressler, "Survey on Coherent Multiband Splicing Techniques for Wideband Channel Characterization," *IET Communications*, vol. 18, no. 19, pp. 1319–1334, Dec. 2024.

[18] M. Noschese, F. Babich, M. Comisso, and C. Marshall, "Multiband time of arrival estimation for long term evolution (LTE) signals," *IEEE Transactions on Mobile Computing*, vol. 20, no. 12, pp. 3383–3394, 2020.

[19] H. Xu, C.-C. Chong, I. Guvenc, F. Watanabe, and L. Yang, “High-resolution TOA estimation with multi-band OFDM UWB signals,” in *IEEE International Conference on Communications (ICC 2008)*, Beijing, China, May 2008, pp. 4191–4196.

[20] Z. Hu, A. Liu, Y. Wan, T. X. Han, and M. Zhao, “A Two-Stage Multiband Delay Estimation Scheme via Stochastic Particle-Based Variational Bayesian Inference,” *IEEE Internet of Things Journal*, Feb. 2024.

[21] Y. Wan, A. Liu, Q. Hu, M. Zhang, and Y. Cai, “Multiband Delay Estimation for Localization Using a Two-Stage Global Estimation Scheme,” *IEEE Transactions on Wireless Communications*, vol. 22, no. 12, pp. 9263–9277, Dec. 2023.

[22] T. Kazaz, R. T. Rajan, G. J. Janssen, and A.-J. Van der Veen, “Multiresolution time-of-arrival estimation from multiband radio channel measurements,” in *IEEE International Conference on Acoustics, Speech and Signal Processing (ICASSP 2019)*, Brighton, United Kingdom, May 2019, pp. 4395–4399.

[23] T. Kazaz, G. J. M. Janssen, and A.-J. van der Veen, “Time Delay Estimation from Multiband Radio Channel Samples in Nonuniform Noise,” in *53rd Asilomar Conference on Signals, Systems, and Computers*, Pacific Grove, CA: IEEE, Nov. 2019.

[24] T. Kazaz, M. Coutino, G. J. Janssen, and A.-J. Van der Veen, “Joint blind calibration and time-delay estimation for multiband ranging,” in *IEEE International Conference on Acoustics, Speech and Signal Processing (ICASSP 2020)*, Barcelona, Spain, May 2020, pp. 4846–4850.

[25] J. Meng, W. Yin, Y. Li, N. T. Nguyen, and Z. Han, “Compressive sensing based high-resolution channel estimation for OFDM system,” *IEEE Journal of Selected Topics in Signal Processing*, vol. 6, no. 1, pp. 15–25, Sep. 2011.

[26] J. Pegoraro, J. O. Lacruz, M. Rossi, and J. Widmer, “HiSAC: High-Resolution Sensing with Multiband Communication Signals,” arXiv, eess.SP 2407.07023, Jul. 2024.

[27] M. B. Khalilsarai, S. Stefanatos, G. Wunder, and G. Caire, “WiFi-based indoor localization via multi-band splicing and phase retrieval,” in *19th IEEE International Workshop on Signal Processing Advances in Wireless Communications (SPAWC 2018)*, Kalamata, Greece, Jun. 2018, pp. 1–5.

[28] S. Dimce, A. Zubow, and F. Dressler, “mmSplicer: Toward Experimental Multiband Channel Splicing at mmWave Frequencies,” in *43rd IEEE International Conference on Computer Communications (INFOCOM 2024), Poster Session*, Vancouver, Canada: IEEE, May 2024.

[29] Z. Tian, Y. Ren, Z. Li, and X. Cheng, “Super-Resolution Time-of-Flight Estimation for Ranging via Multi-Band Splicing,” in *IEEE Global Communications Conference (GLOBECOM 2023)*, Kuala Lumpur, Malaysia, Dec. 2023, pp. 4656–4661.

[30] M. Pourkhaatoun and S. A. Zekavat, “High-resolution low-complexity cognitive-radio-based multiband range estimation: Concatenated spectrum vs. Fusion-based,” *IEEE Systems Journal*, vol. 8, no. 1, pp. 83–92, 2013.

[31] X. Li, H. Wang, Z. Chen, Z. Jiang, and J. Luo, “UWB-Fi: Pushing Wi-Fi towards Ultra-wideband for Fine-Granularity Sensing,” in *Annual International Conference on Mobile Systems, Applications and Services (MobiSys 2024)*, Minato-ku, Tokyo, Japan, Jun. 2024, pp. 42–55.

[32] J. Qiu, P. Zheng, K. Chi, R. Xu, and J. Liu, “Respiration Monitoring in High-Dynamic Environments via Combining Multiple WiFi Channels Based on Wire Direct Connection Between RX/TX,” *IEEE Internet of Things Journal*, vol. 10, no. 3, pp. 1558–1573, Feb. 2023.

[33] S. Shi, Y. Xie, M. Li, A. X. Liu, and J. Zhao, “Synthesizing wider WiFi bandwidth for respiration rate monitoring in dynamic environments,” in *38th IEEE Conference on Computer Communications (INFOCOM 2019)*, Paris, France, Apr. 2019, pp. 181–189.

[34] S. Barrachina-Muñoz, B. Bellalta, and E. W. Knightly, “Wi-Fi channel bonding: An all-channel system and experimental study from urban hotspots to a sold-out stadium,” *IEEE/ACM Transactions on Networking*, vol. 29, no. 5, pp. 2101–2114, Oct. 2021.

[35] M. Pourkhaatoun and S. A. Zekavat, “Concatenated spectrum multi-band TOA estimation,” in *22nd IEEE International Symposium on Personal, Indoor and Mobile Radio Communications (PIMRC 2011)*, Toronto, Canada, Sep. 2011, pp. 1192–1196.

[36] Y. Wan, Z. Hu, A. Liu, R. Du, T. X. Han, and T. Q. Quek, “OFDM-Based Multiband Sensing For ISAC: Resolution Limit, Algorithm Design, and Open Issues,” *IEEE Vehicular Technology Magazine*, Jun. 2024.

[37] S. Dimce, A. Zubow, A. Bayesteh, G. Caire, and F. Dressler, “Practical Channel Splicing using OFDM Waveforms for Joint Communication and Sensing in the IoT,” arXiv, cs.NI 2305.05508, May 2023.

[38] W. Chen, Y. Han, S. Jin, and H. Sun, “Efficient multiband channel reconstruction and tracking for hybrid mmWave MIMO systems,” *IEEE Transactions on Communications*, vol. 69, no. 12, pp. 8501–8517, 2021.

[39] C. Chen, Y. Chen, Y. Han, H.-Q. Lai, and K. R. Liu, “Achieving centimeter-accuracy indoor localization on WiFi platforms: A frequency hopping approach,” *IEEE Internet of Things Journal*, vol. 4, no. 1, pp. 111–121, 2016.

[40] Z. Hu, A. Liu, Y. Wan, T. Q. S. Quek, and M.-J. Zhao, “Two-stage Multiband Wi-Fi Sensing for ISAC via Stochastic Particle-Based Variational Bayesian Inference,” in *IEEE Global Communications Conference (GLOBECOM 2023)*, Kuala Lumpur, Malaysia: IEEE, Dec. 2023.

[41] Y. Zhuo, H. Zhu, H. Xue, and S. Chang, “Perceiving accurate CSI phases with commodity WiFi devices,” in *36th IEEE Conference on Computer Communications (INFOCOM 2017)*, Atlanta, GA: IEEE, May 2017.

[42] A. Ghosh and M. Kim, “THz channel sounding and modeling techniques: An overview,” *IEEE Access*, vol. 11, pp. 17 823–17 856, 2023.

[43] S. J. Wright, R. D. Nowak, and M. A. Figueiredo, “Sparse reconstruction by separable approximation,” *IEEE Transactions on Signal Processing*, vol. 57, no. 8, pp. 2479–2493, Jul. 2009.

[44] T. S. Rappaport, *Wireless Communications: Principles and Practice*. Upper Saddle River, NJ: Prentice Hall, 1996.

[45] J. Heiskala and J. Terry, *OFDM Wireless LANs: A Theoretical and Practical Guide*. Indianapolis, IN: SAMS, 2001.

[46] R. Sun, P. B. Papazian, J. Senic, Y. Lo, J.-K. Choi, K. A. Remley, and C. Gentile, “Design and calibration of a double-directional 60 GHz channel sounder for multipath component tracking,” in *11th European Conference on Antennas and Propagation (EUCAP 2017)*, Paris, France: IEEE, Mar. 2017, pp. 3336–3340.

[47] C. Lv, J.-C. Lin, and Z. Yang, “Channel prediction for millimeter wave MIMO-OFDM communications in rapidly time-varying frequency-selective fading channels,” *IEEE Access*, pp. 15 183–15 195, Jan. 2019.

[48] A. Le Ha, T. Van Chien, T. H. Nguyen, W. Choi, and V. Duc Nguyen, “Deep Learning-Aided 5G Channel Estimation,” in *15th International Conference on Ubiquitous Information Management and Communication (IMCOM 2021)*, Seoul, South Korea: IEEE, Jan. 2021, pp. 1–7.

[49] D. Garcia, R. Ruiz, J. O. Lacruz, and J. Widmer, “High-speed Machine Learning-enhanced Receiver for Millimeter-Wave Systems,” in *42nd IEEE International Conference on Computer Communications (INFOCOM 2023)*, New York City, NY, May 2023, pp. 1–10.

[50] J. Zhu, C.-k. Wen, J. Tong, C. Xu, and S. Jin, “Grid-less variational Bayesian channel estimation for antenna array systems with low resolution ADCs,” *IEEE Transactions on Wireless Communications*, vol. 19, no. 3, pp. 1549–1562, Mar. 2020.

[51] L. Wan, J. Zhu, E. Cheng, and Z. Xu, “Joint CFO, gridless channel estimation and data detection for underwater acoustic OFDM systems,” *IEEE Journal of Oceanic Engineering*, vol. 47, no. 4, pp. 1215–1230, 2022.

[52] M. Xu, J. Zhu, J. Fang, N. Zhang, and Z. Xu, “CFAR based NOMP for line spectral estimation and detection,” *IEEE Transactions on Aerospace and Electronic Systems*, vol. 59, no. 5, pp. 6971–6990, 2023.

[53] N. U. R. Junejo, H. Esmaiel, M. Zhou, H. Sun, J. Qi, and J. Wang, “Sparse channel estimation of underwater TDS-OFDM system using look-ahead backtracking orthogonal matching pursuit,” *IEEE Access*, vol. 6, pp. 74 389–74 399, Nov. 2018.

[54] W. Ding, F. Yang, C. Pan, L. Dai, and J. Song, “Compressive sensing based channel estimation for OFDM systems under long delay channels,” *IEEE Transactions on Broadcasting*, vol. 60, no. 2, pp. 313–321, 2014.

[55] L. Dai, J. Wang, Z. Wang, P. Tsiaflakis, and M. Moonen, “Spectrum-and energy-efficient OFDM based on simultaneous multi-channel reconstruction,” *IEEE Transactions on Signal Processing*, vol. 61, no. 23, pp. 6047–6059, 2013.

[56] H. Dun, C. C. Tiberius, C. Diouf, and G. J. Janssen, “Sparse signal bands selection for precise time-based ranging in terrestrial posi-

tioning," in *IEEE/ION Position, Location and Navigation Symposium (PLANS 2020)*, Portland, OR, Apr. 2020, pp. 1372–1380.

[57] E. C. Marques, N. Maciel, L. Naviner, H. Cai, and J. Yang, "A review of sparse recovery algorithms," *IEEE Access*, vol. 7, pp. 1300–1322, Dec. 2018.

[58] S. Kwon, J. Wang, and B. Shim, "Multipath Matching Pursuit," *IEEE Transactions on Information Theory*, vol. 60, no. 5, pp. 2986–3001, May 2014.

[59] Z. Yang and L. Xie, "On gridless sparse methods for line spectral estimation from complete and incomplete data," *IEEE Transactions on Signal Processing*, vol. 63, no. 12, pp. 3139–3153, 2015.

[60] T. H. Cormen, C. E. Leiserson, R. L. Rivest, and C. Stein, *Introduction to algorithms*. MIT Press, 2022.

[61] S. Arora and B. Barak, *Computational Complexity: A Modern Approach*. Cambridge University Press, 2009, p. 608.

Sigrid Dimce is a Researcher at the Telecommunications Networks Group (TKN) at TU Berlin, Germany, which she joined in May 2020. She received her M.Sc. in Computer Engineering from Paderborn University, Germany, in 2020, and her B.Sc. in Telecommunication Engineering from Polytechnic University of Tirana, Albania, in 2014. Her research focuses on millimeter-wave (mmWave) communications, and wide-band channel characterization,

Anatolij Zubow received his M.Sc. in computer science (2004) and Ph.D.(2009) from Humboldt University Berlin. He is a senior researcher at the Telecommunication Networks Group at the Technische Universität Berlin since March 2013, where he is coordinating the research activities in the areas of cognitive radio, wireless access networks, and software-defined networking. In the past he did research in the area of wireless ad hoc mesh and self-organized networks.

Alireza Bayesteh received the B.Sc. and M.Sc. degrees from the Sharif University of Technology, Iran, in 2000 and 2002, respectively, and the Ph.D. degree in electrical and computer engineering from the University of Waterloo, Canada, in 2008. From 2008 to 2009, he was a Postdoctoral Fellow with the University of Waterloo. From 2009 to 2011, he was a Member of Technical Staff with Research In Motion (currently BlackBerry Ltd.). Since 2011, he has been with Huawei Canada, Ottawa, where he is currently a Senior Principal Engineer. His research interest includes various aspects of air interface design for 6G wireless communications.

Giuseppe Caire (S '92 – M '94 – SM '03 – F '05) was born in Torino in 1965. He received a B.Sc. in Electrical Engineering from Politecnico di Torino in 1990, an M.Sc. in Electrical Engineering from Princeton University in 1992, and a Ph.D. from Politecnico di Torino in 1994. He has been a postdoctoral research fellow with the European Space Agency (ESTEC, Noordwijk, The Netherlands) in 1994-1995, Assistant Professor in Telecommunications at the Politecnico di Torino, Associate Professor at the University of Parma, Italy, Professor with the Department of Mobile Communications at the Eurecom Institute, SophiaAntipolis, France, a Professor of Electrical Engineering with the Viterbi School of Engineering, University of Southern California, Los Angeles, and he is currently an Alexander von Humboldt Professor with the Faculty of Electrical Engineering and Computer Science at the Technical University of Berlin, Germany. He received the Jack Neubauer Best System Paper Award from the IEEE Vehicular Technology Society in 2003, the IEEE Communications Society and Information Theory Society Joint Paper Award in 2004 and in 2011, the Okawa Research Award in 2006, the Alexander von Humboldt Professorship in 2014, the Vodafone Innovation Prize in 2015, an ERC Advanced Grant in 2018, the Leonard G. Abraham Prize for best IEEE JSAC paper in 2019, the IEEE Communications Society Edwin Howard Armstrong Achievement Award in 2020, the 2021 Leibniz Prize of the German National Science Foundation (DFG), and the CTTC Technical Achievement Award of the IEEE Communications Society in 2023. Giuseppe Caire is a Fellow of IEEE since 2005. He has served in the Board of Governors of the IEEE Information Theory Society from 2004 to 2007, and as officer from 2008 to 2013. He was President of the IEEE Information Theory Society in 2011. His main research interests are in the field of communications theory, information theory, channel and source coding with particular focus on wireless communications.

Falko Dressler (F'17) received the M.Sc. and Ph.D. degrees from the Department of Computer Science, University of Erlangen, in 1998 and 2003, respectively. He is currently a Full Professor and the Chair of Telecommunication Networks with the School of Electrical Engineering and Computer Science, TU Berlin. Dr. Dressler has been associate editor-in-chief for IEEE Trans. on Network Science and Engineering, IEEE Trans. on Mobile Computing and Elsevier Computer Communications as well as an editor for journals such as IEEE/ACM Trans. on Networking, Elsevier Ad Hoc Networks, and Elsevier Nano Communication Networks. He has been chairing conferences such as IEEE INFOCOM, ACM MobiSys, ACM MobiHoc, IEEE VNC, IEEE GLOBECOM. He authored the textbooks Self-Organization in Sensor and Actor Networks published by Wiley & Sons and Vehicular Networking published by Cambridge University Press. He has been an IEEE Distinguished Lecturer as well as an ACM Distinguished Speaker. Dr. Dressler is an IEEE Fellow, an ACM Fellow, and an AAIA Fellow. He is a member of the German National Academy of Science and Engineering (acatech). He has been serving on the IEEE COMSOC Conference Council and the ACM SIGMOBILE Executive Committee. His research objectives include next generation wireless communication systems in combination with distributed machine learning and edge computing for improved resiliency. Application domains include the internet of things, cyber-physical systems, and the internet of bio-nano-things.